Technical Note

Crystal Growth of MICP through Microfluidic Chip Tests

Yang Xiao, Ph.D., M.ASCE[1]; Xiang He, S.M.ASCE[2]; Armin W. Stuedlein, Ph.D., P.E., M.ASCE[3]; Jian Chu, Ph.D., M.ASCE[4]; T. Matthew Evans, Ph.D., M.ASCE[5]; and Leon A. van Paassen, M.ASCE[6]

Abstract: A significant pressing issue in microbially induced calcium carbonate precipitation (MICP) is the characterization of the heterogeneous growth mechanics of calcium carbonate ($CaCO_3$) crystals. This study aimed to visualize the bacteria and $CaCO_3$ distributions at the quiescent state through microfluidic chip tests where the bacterial solution (BS) and cementation solution (CS) were initially injected simultaneously from two separate microchannels and subsequently converged in a reaction microchannel. The experiments revealed that the bacterial diffusion within the CS injection area was hindered for a high concentration of calcium chloride ($CaCl_2$) (e.g., 0.5 M), whereas diffusion appeared homogeneous for a low concentration of $CaCl_2$ (0.05 M). In addition, the $CaCO_3$ distribution along the width of the reaction microchannel was more uniform for 0.05 M $CaCl_2$ than for 0.5 M $CaCl_2$. The microfluidic chip tests in this study provided kinetic observations of the MICP process that improved the understanding of the mechanics of bacterial diffusion and $CaCO_3$ crystal growth and their variation with different concentrations of $CaCl_2$. **DOI: 10.1061/(ASCE)GT.1943-5606.0002756.**

Introduction

Microbially induced calcium-carbonate precipitation (MICP) (DeJong et al. 2006; Whiffin et al. 2007; van Paassen et al. 2010b) provides a promising ground-improvement alternative to traditional techniques and may be used to increase strength and dilatancy (Chou et al. 2011; Montoya and DeJong 2015; Venda Oliveira et al. 2015; Cui et al. 2017; Gomez et al. 2018; Mahawish et al. 2019b; Xiao et al. 2019b), improve liquefaction resistance (Montoya et al. 2013; Feng and Montoya 2017; O'Donnell et al. 2017; Darby et al. 2019; Xiao et al. 2019a; Riveros and Sadrekarimi 2020; Wang et al. 2020; Xiao et al. 2021), decrease hydraulic conductivity (Chu et al. 2013; Cheng et al. 2017), reduce compressibility (van Paassen et al. 2010a; Lin et al. 2016a; Liu et al. 2019; Montoya et al. 2019), increase thermal conductivity (Venuleo et al. 2016; Martinez et al. 2019), control erosion (Jiang et al. 2017; Ham et al. 2018; Fattahi et al. 2020), restrain particle breakage (Xiao et al. 2020a), heal cracks (El Mountassir et al. 2014; Tobler et al. 2018; Minto et al. 2019), and increase the bearing capacity of piles (Lin et al. 2016b; Xiao et al. 2020b). Most prior studies have been conducted at the element scale and have not to provide robust insight into the underlying microscale physics that govern the macroscale manifestation of MICP.

Microfluidics have been used to investigate the kinetics of calcium carbonate ($CaCO_3$) mineralization (Zhang et al. 2010; Song et al. 2018; Yoon et al. 2019). Recently, Wang et al. (2019a) designed a synthetic porous microfluidic chip to observe the pore-scale behavior of bacteria and $CaCO_3$ crystals during MICP. Furthermore, Wang et al. (2019b) moved to qualitatively evaluate the influence of the injection interval on the size and quantity of $CaCO_3$ crystals. In addition, Kim et al. (2020) investigated the kinetic precipitation of $CaCO_3$ crystals in the process of enzymatically induced calcium-carbonate precipitation (EICP) via microfluidic tests, which was captured by a simple crystal growth model. These investigations demonstrated the potential of microfluidics for the evaluation of the kinetics of biomineralization. This study aimed to investigate the diffusion and motility of bacterial in relation to the growth kinetics of $CaCO_3$ in the MICP process using a microfluidic chip with two inlet ports. Bacterial and $CaCO_3$ distributions and single crystal growth in the reaction microchannel were observed and evaluated under varying concentrations of calcium chloride ($CaCl_2$) to advance the understanding of crystal growth and improve those processes governing optimal application of MICP.

Experimental Materials and Protocols

Bacterial Solution and Cementation Solution

The bacteria *Sporosarcina pasteurii* (American Type Culture Collection 11859) were used to produce urease and are cultivated in a sterile liquid medium (Xiao et al. 2019b) for 36 h. The harvested bacteria are centrifuged at 7,000 g for 14 min at 4°C and resuspended in a 0.85% NaCl solution. The bacterial solution (BS) with an optical density of 0.14 was obtained by diluting the resuspended solution 10 times. For fluorescence observation, the bacteria were stained with a bacterial viability kit (BacLight Kit, L-7012, Invitrogen, Carlsbad, California) following the procedures proposed by Boulos et al. (1999), where 1.5 μL dye medium was added into

[1]Professor, Key Laboratory of New Technology for Construction of Cities in Mountain Area, State Key Laboratory of Coal Mine Disaster Dynamics and Control, School of Civil Engineering, Chongqing Univ., Chongqing 400045, China (corresponding author). ORCID: https://orcid.org/0000-0002-9411-4660. Email: hhuxyanson@163.com

[2]Ph.D. Candidate, School of Civil Engineering, Chongqing Univ., Chongqing 400045, China. Email: medihe@163.com

[3]Professor, School of Civil and Construction Engineering, Oregon State Univ., Corvallis, OR 97331. Email: Armin.Stuedlein@oregonstate.edu

[4]Professor, School of Civil and Environmental Engineering, Nanyang Technological Univ., Singapore 639798. Email: cjchu@ntu.edu.sg

[5]Professor, School of Civil and Construction Engineering, Oregon State Univ., Corvallis, OR 97331. ORCID: https://orcid.org/0000-0002-8457-7602. Email: matt.evans@oregonstate.edu

[6]Associate Professor, Center for Biomediated and Bioinspired Geotechnics, Arizona State Univ., Tempe, AZ 85287-3005. Email: leon.vanpaassen@asu.edu

Note. This manuscript was submitted on August 29, 2020; approved on November 22, 2021; published online on February 16, 2022. Discussion period open until July 16, 2022; separate discussions must be submitted for individual papers. This technical note is part of the ***Journal of Geotechnical and Geoenvironmental Engineering***, © ASCE, ISSN 1090-0241.

1 mL BS for 15 min of incubation in the absence of ambient light. The physiochemical properties of the bacteria membrane are not affected by fluorescence staining (Robertson et al. 2019). We evaluated three cementation solutions (CS), including one composed of 0.5 M urea and 0.05 M $CaCl_2$ (a low concertation of calcium ions), one composed of 0.5 M urea and 0.1 $CaCl_2$ (an intermediate concertation of calcium ions), and one composed of 0.5 M urea and 0.5 $CaCl_2$ (a high concertation of calcium ions) to study the effect of $CaCl_2$ on the homogeneity and quantity of crystal growth.

Microfluidic System

Fig. 1(a) shows the microfluidic system that consists of two programmable syringe pumps (Pump 11 Elite 4501, Harvard, Holliston, Massachusetts), a micromodel, a temperature control system, and an imaging system. The syringe pumps were used to inject the BS and CS into the micromodel separately from the two inlets. The temperature control system was used to maintain the temperature at 25°C during the reaction periods. The imaging system was equipped with an inverted fluorescence microscope (IX73, Olympus, Tokyo), a camera (DP74, Olympus), and a computer for image collection and storage. The micromodel, microscope, and pumps were insulated in a dark chamber to avoid light interference. Fig. 1(b) shows the fabrication processes of the microchip, and the detailed procedures are introduced in the Supplemental Materials and shown in Figs. S1–S4 and Video S1. The reaction microchannel was 8,000 μm in length, 950 μm in width, and 120 μm in depth, and the two inlet microchannels were 5,600 μm in length, 450 μm in width, and 120 μm in depth [Fig. 1(c)].

Procedures of Microfluidic Chip Tests

Prior to testing, the air in microchannels was expelled by injecting deaired water with a flow rate of 100 μL/h. Six experiments with different concentrations of $CaCl_2$ and injection quantities were conducted to investigate bacterial diffusion and $CaCO_3$ precipitation, as listed in Table 1. The BS and CS were then injected through two separate inlet microchannels with a flow rate of 40 μL/h (i.e., a corresponding Darcy velocity of 0.98×10^{-4} m/s). After injection with approximately seven pore volumes of the reaction channel, the two pumps and exit valve were closed to maintain a quiescent state where the bacterial cells, urea, and calcium ions were subject to diffusion and reaction processes for 2.5 h. This period is termed an injection interval for multiple-injection tests. The effluent after each injection interval was discharged from the outlet of the reaction microchannel.

Tests using different concentrations of $CaCl_2$ with one injection (i.e., T-H-1, T-I-1, and T-L-1) were used to investigate the influence of $CaCl_2$ concentration on bacterial distribution, whereas tests with multiple injections (i.e., T-H-10, T-I-10, and T-L-10) were used to explore the influence of $CaCl_2$ concentration on the size and shape of typical $CaCO_3$ crystals and the evolution and distribution of $CaCO_3$ precipitates along the width and length of the reaction microchannel. Both bacterial solution and cementation solution were injected 10 times in the T-H-10, T-I-10, and T-L-10.

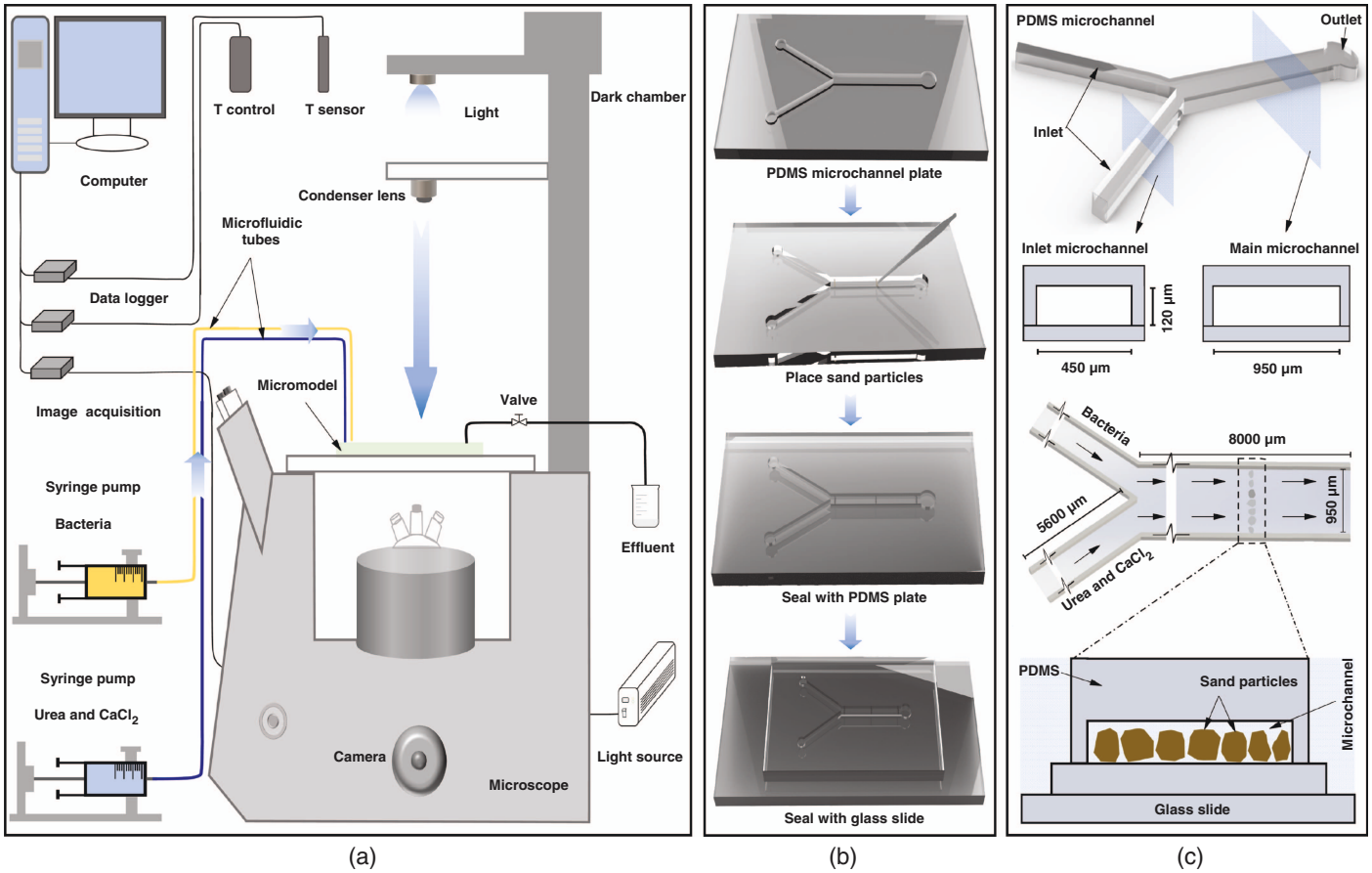

Fig. 1. (Color) Setup of microfluidic chip tests: (a) schematics of microfluidic system; (b) schematic fabrication process of micromodel; and (c) length, width, and depth of the reaction microchannel and two inlet microchannels. In T control and T sensor, T denotes temperature.

J. Geotech. Geoenviron. Eng., 2022, 148(5): 06022002

Table 1. Test parameters and concentrations of cementation solutions in microfluidic tests

Protocol	Urea	$CaCl_2$	N	t_i	t_t
T-H-1	0.5	0.5	1	—	2.5
T-I-1	0.5	0.1	1	—	2.5
T-L-1	0.5	0.05	1	—	2.5
T-H-10	0.5	0.5	10	2.5	25
T-I-10	0.5	0.1	10	2.5	25
T-L-10	0.5	0.05	10	2.5	25

Note: In T-x-N, x = H, I, or L denoting high, moderate, or low concentration of $CaCl_2$, respectively; N = injection number of tests; and t_i and t_t = injection interval and total treatment time (h). The unit for urea and $CaCl_2$ is mol/L.

Image Acquisition and Processing

All experimental images were obtained using an inverted microscope (IX73, Olympus) with a 10× objective. For the single-injection tests, the green fluorescence imagery was captured by a camera and then converted to a grayscale image. All of the fluorescence images with a width of 950 μm (i.e., the width of the reaction microchannel) and length of 1,220 μm (around the row of sand grains) were centered at the middle depth of the microchannel. Three rectangular areas (245 μm in length) designated as the Entry, Sand, and Exit Sample Windows were selected for evaluation and are identified by the dashed lines in Fig. 2.

For the multiple-injection tests, the growth of $CaCO_3$ crystals in the MICP process during the whole reaction period (1,500 min) was captured through a bright-field imaging mode. The bright-field image size was the same as that of the fluorescence image, whereas the bright-field image position changed along the depth of the reaction microchannel for improved acquisition of $CaCO_3$ crystal profiles (Singh et al. 2017). The methods used to quantify the bacterial cells and $CaCO_3$ crystals are provided in the Supplemental Materials and shown in Figs. S5 and S6.

Experimental Results and Discussion

Distribution of Bacteria

Fig. 2 presents the grayscale images of bacteria at the beginning and after the 10th min of BS and CS injections with different concentrations of $CaCl_2$, which were observed from the top of the reaction microchannel. The living bacterial cells are visible as open spots in the grayscale images as a result of the imposed fluorescence, which facilitates ocular inspection and quantification of the cells to estimate the diffusion of the bacteria (Okumus et al. 2018; Robertson et al. 2019; Rossy et al. 2019). As shown in Figs. 2(a, e, and i), a similar distribution of bacteria may be observed for different $CaCl_2$ concentrations at the initiation of injection, where almost all of the bacterial cells are located in the BS-injection area (i.e., the bottom half of the image). However, the bacterial cells in Figs. 2(c, g, and k) showed clear distinctions

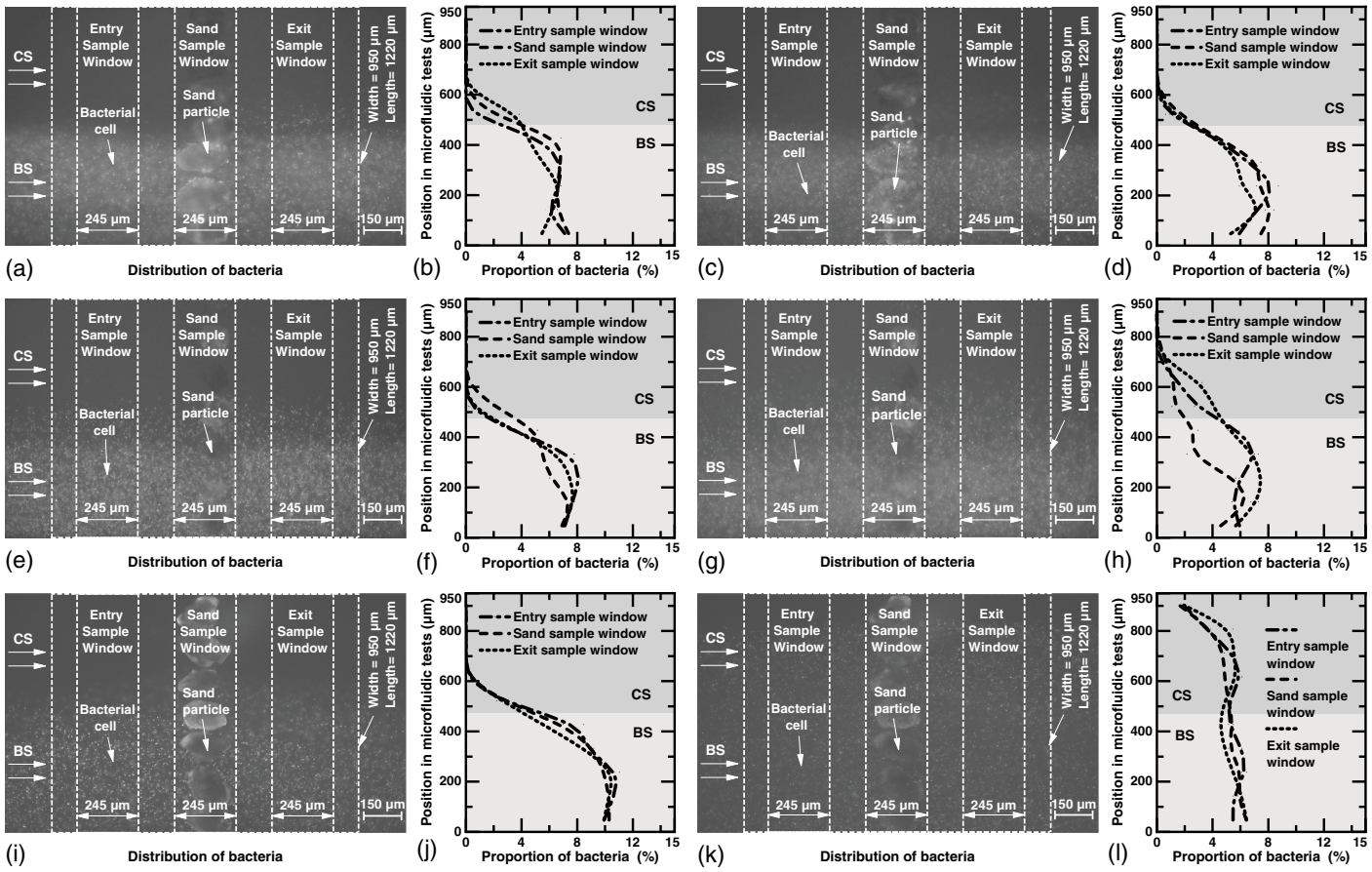

Fig. 2. Bacteria distribution and proportion: (a–d) beginning and tenth minute for 0.5 M $CaCl_2$; (e–h) beginning and tenth minute for 0.1 M $CaCl_2$; and (i–l) beginning and tenth minute for 0.05 M $CaCl_2$.

J. Geotech. Geoenviron. Eng., 2022, 148(5): 06022002

among the three $CaCl_2$ concentrations evaluated. For the 0.5 M concentration of $CaCl_2$, the bacterial cells at the 10th min were similarly distributed as that at the initiation of injection, whereas for the 0.05 M concentration of $CaCl_2$, the distribution of bacterial cells was relatively uniform along the width of the microchannel at the 10th min. These observations indicated that high concentrations of $CaCl_2$ can restrict the mobility of bacteria and stimulate flocculation and adsorption of bacterial cells (Kim 1996; Harkes et al. 2010; Licata et al. 2016).

Each of the sample windows (i.e., Entry Sample Window, Sand Sample Window, and Exit Sample Window) was divided into 10 subareas along the width of the reaction microchannel to calculate the proportion of bacteria within a subarea relative to the total area comprising each of the three sample windows. The distribution of bacteria across the width of the reaction microchannel may be represented as proportion of bacterial cells for a given position of a subarea, with the center of each subarea selected to represent its position. Figs. 2(b, d, f, h, j, and l) present such distributions for various reaction periods and $CaCl_2$ concentrations. An interesting finding in the comparison of Figs. 2(d, h, and l) is that the uniformity of bacterial cells increased as the concentrations of $CaCl_2$ decreased. For example, the distribution of bacteria along the width of the reaction microchannel was more uniform for 0.05 M $CaCl_2$ than for 0.5 M $CaCl_2$ at the 10th min. In addition, the difference in accumulated bacteria in Entry Sample Window, Sand Sample Window, and Exit Sample Window was marginal regardless of the $CaCl_2$ concentration, which indicated that sand grains did not exhibit an obvious preferred adsorption of bacterial cells. However, this observation appears to refute the previous hypothesis that bacterial cells attach to the surfaces or contacts of sand grains for further precipitation of $CaCO_3$ (Torkzaban et al. 2008; Foppen et al. 2010).

Distribution of $CaCO_3$ *Precipitates*

Fig. 3 presents the evolution of $CaCO_3$ precipitation at different reaction periods obtained from microvideography during the microfluidic experiments (Video S2 shows 0.5 M $CaCl_2$, Video S3 shows 0.1 M $CaCl_2$, and Video S4 shows 0.05 M $CaCl_2$, respectively). To improve interpretation, the reaction microchannel background, sand particles, and $CaCO_3$ crystals are rendered in gray, light yellow, and magenta, respectively, in Fig. 3. The distribution of $CaCO_3$ precipitation differed significantly for the three $CaCl_2$ concentrations evaluated, with significantly greater uniformity across the width (950 μm) of the observed area as the concentration of $CaCl_2$ increases. For 0.5 M $CaCl_2$ in Fig. 3(d), most of $CaCO_3$ precipitates were observed along the BS-injection flow path, implying that the urea and calcium ions diffused into this flow path owing to the retention of bacteria there, as observed in Figs. 2(a–d). The comparatively uniform distribution of $CaCO_3$ precipitates for the 0.05 M concentration of $CaCl_2$ in Fig. 3(l) demonstrates that the urea and calcium ions spread uniformly along the width of the microchannel because the bacteria were uniformly distributed along the width of the reaction microchannel, as observed in Figs. 2(i–l).

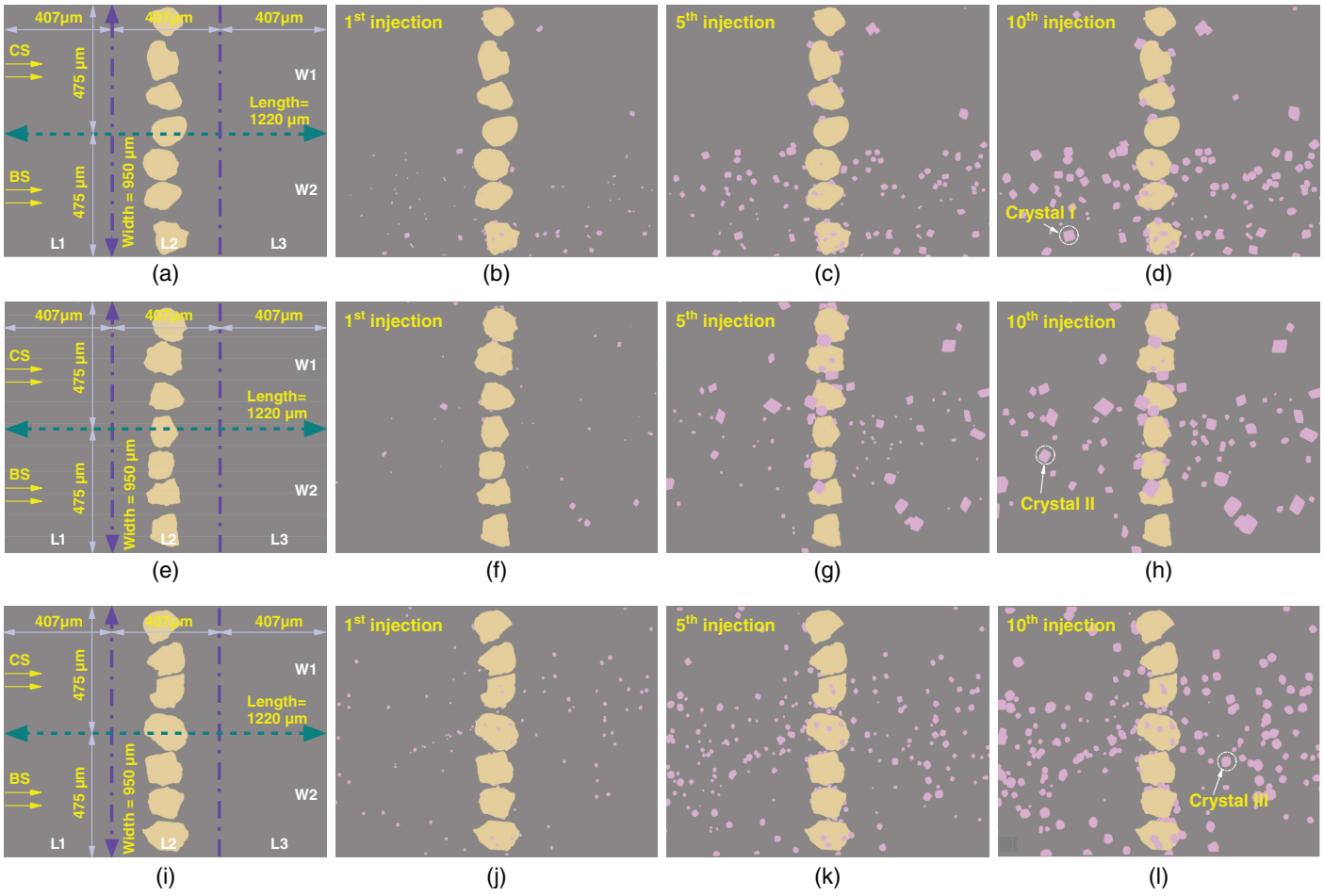

Fig. 3. (Color) Evolution and distribution of $CaCO_3$ precipitates: (a–d) beginning, 150th, 750th, and 1,500th min for 0.5 M $CaCl_2$; (e–h) beginning, 150th, 750th, and 1,500th min for 0.1 M $CaCl_2$; and (i–l) beginning, 150th, 750th, and 1,500th min for 0.5 M $CaCl_2$.

J. Geotech. Geoenviron. Eng., 2022, 148(5): 06022002

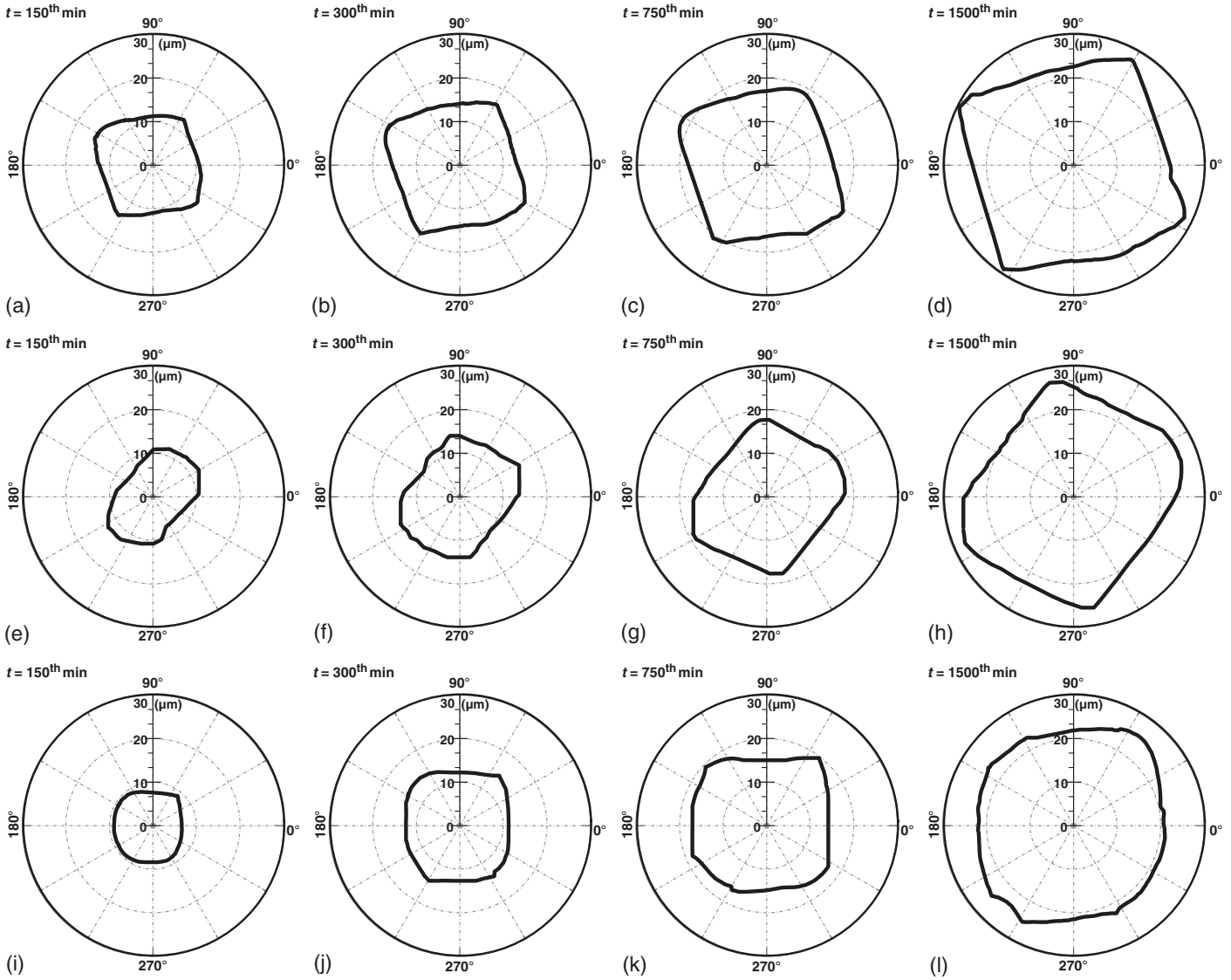

Fig. 4. (a–d) $CaCO_3$ crystal growth for 0.5 M $CaCl_2$ at different treatment stages; (e–h) $CaCO_3$ crystal growth for 0.1 M $CaCl_2$ at different treatment stages; and (i–l) $CaCO_3$ crystal growth for 0.05 M $CaCl_2$ at different treatment stages.

The microfluidic experiments allowed quantification of the crystal growth and morphology in the reaction microchannel. The methods used for quantification of $CaCO_3$ crystals are provided in the Supplemental Materials. The morphology of single crystals can be determined using Eqs. (S1) and (S2). Figs. 4(a–d, e–h, and i–l) show the growth of a single crystal, i.e., Crystals I, II, and III (marked in Fig. 3), for 0.5, 0.1, and 0.05 M $CaCl_2$, respectively. The vertical coordinates in Fig. 4 denote the size of the three crystals in micrometers. As shown in Figs. 4(a, e, and i), the projected area of Crystal I at the 150th min after the first injection was approximately 1.6 times that of Crystal II and 2.1 times that of Crystal III. By the 1,500th min, the projected area of Crystal I was slightly larger than that of Crystals II and III, as shown in Figs. 4(d, h, and l). Interestingly, the $CaCO_3$ crystal morphology during the precipitation was similar at different reaction periods for both concentrations of $CaCl_2$ evaluated, indicating that the crystal morphology was unchanged once the steady crystal formed at the quiescent state, which was also reported by Wang et al. (2019a).

Figs. 5(a–c) show the evolution of the cumulative distributions of the $CaCO_3$ crystal areas for different $CaCl_2$ concentrations. The cumulative distributions at different reaction periods were approximately parallel for all $CaCl_2$ concentrations evaluated. Mean crystal area A_{50} is defined as the crystal area where 50% of the crystals are finer (i.e., smaller). The A_{50} increased as the reaction period increased regardless of $CaCl_2$ concentrations. A higher concentration of $CaCl_2$ produced a larger A_{50} with the same reaction period, indicating that $CaCO_3$ crystal grew faster in a high concentration of $CaCl_2$ than in a low concentration of $CaCl_2$.

The observed area in Figs. 3(a, e, and i) is divided into two equal parts, the CS injection area (denoted as Subarea W_1 with a width of 475 μm) and the BS-injection area (denoted as Subarea W_2 with a width of 475 μm), along the width of the reaction microchannel, or three equal parts (denoted as Subareas L_1, L_2, and L_3 with lengths of 407 μm) along the length of the reaction microchannel to quantitatively estimate the distributions of $CaCO_3$ precipitates. The proportion of $CaCO_3$ in one subarea was defined as the ratio of projected area of $CaCO_3$ precipitates in this subarea to that in the total observed area [950 μm in width and 1220 μm in length in Fig. 3(a)], which can be expressed in detail as follows:

J. Geotech. Geoenviron. Eng., 2022, 148(5): 06022002

$$P_{Ca}^{w1} = A_{Ca}^{w1}/A_{Ca}^{t}, \quad P_{Ca}^{w2} = A_{Ca}^{w2}/A_{Ca}^{t}$$
$$P_{Ca}^{l1} = A_{Ca}^{l1}/A_{Ca}^{t}, \quad P_{Ca}^{l2} = A_{Ca}^{l2}/A_{Ca}^{t}, \quad P_{Ca}^{l3} = A_{Ca}^{l3}/A_{Ca}^{t} \quad (1)$$

where P_{Ca}^{w1}, P_{Ca}^{w2}, P_{Ca}^{l1}, P_{Ca}^{l2}, and P_{Ca}^{l3} = proportion of $CaCO_3$ in Subareas W_1, W_2, L_1, L_2, and L_3, respectively; and A_{Ca}^{w1}, A_{Ca}^{w2}, A_{Ca}^{l1}, A_{Ca}^{l2}, A_{Ca}^{l3}, and A_{Ca}^{t} = projected area of $CaCO_3$ precipitates in Subareas W_1, W_2, L_1, L_2, and L_3, and total observed area, respectively.

Figs. 5(d–i) show that the proportion of $CaCO_3$ in different subareas for different $CaCl_2$ concentrations tended to stabilize from approximately the 400th min. Generally, the formation of $CaCO_3$ crystals consists of two stages: nucleation and growth. Nucleation of new crystals requires a significantly high supersaturation of calcium and carbonate ions, and the growth rate and growth mechanism defining the mineral type and crystal shape are directly related to the supersaturation, the available surface area for crystal growth, and relative concentrations of the two precipitating ions (van Paassen 2009; Kim et al. 2020). Changes in the proportion of $CaCO_3$ occurred prior to the 400th min in the selected subareas, which could possibly be attributed to the dissolution of the irregularly shaped and less stable $CaCO_3$ and also the phase transformation of $CaCO_3$, as observed in the glass slide and microfluidic chip tests by Wang et al. (2019b), or because there was not enough crystal surface area available, which stimulated crystal nucleation over crystal growth (Kim et al. 2020). After the 400th min, the growth of existing $CaCO_3$ crystals dominated over the nucleation of new $CaCO_3$ crystals, resulting in a fixed distribution of $CaCO_3$ in the selected subareas, which agrees with the findings by Nayanthara et al. (2019).

As shown in Figs. 5(d–f), the stable value of P_{Ca}^{w2} in Subarea W_2 was at least six times larger than that of P_{Ca}^{w1} in Subarea W_1 for 0.5 M $CaCl_2$, whereas the stable difference between the two subareas for 0.1 M $CaCl_2$ reduced to approximately 1.8 times and for 0.05 M $CaCl_2$ reduced to approximately 1.5 times. In addition, the difference of the proportion of $CaCO_3$ in Subareas L_1, L_2, and L_3 was much larger for a high concentration of $CaCl_2$ than for a low concentration of $CaCl_2$ beginning at a reaction period of approximately 130 min, as shown in Figs. 5(g–i). Consequently, the distribution of $CaCO_3$ precipitates in the microfluidic chip tests was more uniform for a low concentration of $CaCl_2$ than for a high

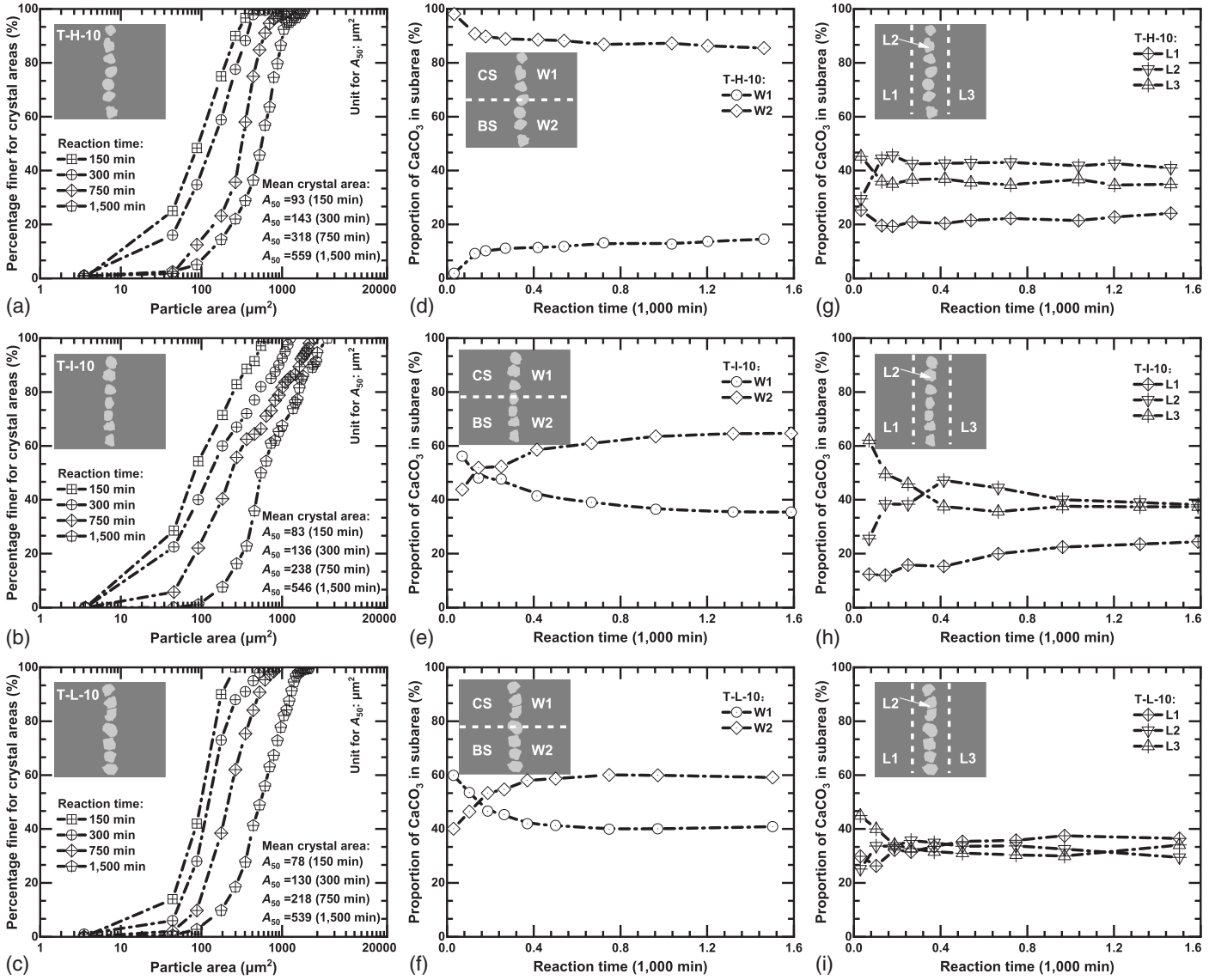

Fig. 5. (a–c) Evolution of the cumulative distribution of the $CaCO_3$ crystal areas for different concentrations of $CaCl_2$; and (d–i) proportion of the $CaCO_3$ crystal areas along the width and length of reaction microchannel for different concentrations of $CaCl_2$.

J. Geotech. Geoenviron. Eng., 2022, 148(5): 06022002

concentration of $CaCl_2$, which agrees with findings from macroscale laboratory tests (Al Qabany and Soga 2013; Martinez et al. 2013; Mahawish et al. 2019a).

The amount of $CaCO_3$ precipitates around sand particles in Subarea L_2 was a little larger than that in Subareas L_1 and L_3 for 0.5 M $CaCl_2$ but the difference in the proportion of $CaCO_3$ in Subareas L_2 and L_3 became small with increasing reaction period, as shown in Fig. 5(g). Furthermore, the difference in the distribution of $CaCO_3$ precipitates in Subareas L_1, L_2, and L_3 for 0.05 M $CaCl_2$ was negligible, implying that $CaCO_3$ does not preferentially precipitate around sand grains (Cheng and Shahin 2016). Such observations should be compared against further microfluidic chip tests with multiple rows of sand grains to assess the role of more tortuous flow paths and corresponding grain–fluid interactions to confirm the preference, or lack thereof, of precipitation on or in proximity to the sand grains.

Conclusions

This study investigated the kinetics of bacterial diffusion and $CaCO_3$ precipitation for two different $CaCl_2$ concentrations through a series of microfluidic chip tests. Microvideography enabled quantification of the distribution of bacteria and $CaCO_3$ precipitates along the width and length of the reaction microchannel. The main conclusions of this study include the following:

- The distribution of bacteria along the width of the reaction microchannel was more uniform for high concentration of $CaCl_2$ than for low concentration of $CaCl_2$ at the 10th min, indicating that a high concentration of $CaCl_2$ restricted the diffusion of bacteria to the area occupied by the cementation solution. The distribution of bacteria along the length of the reaction microchannel was relatively uniform regardless of high or low concentration of $CaCl_2$.
- According to the evolution of the mean crystal area, $CaCO_3$ crystal grew faster in a high concentration of $CaCl_2$ than in a low concentration of $CaCl_2$. A more heterogeneous distribution of $CaCO_3$ precipitates was observed along the width of the reaction microchannel for the high concentration of $CaCl_2$ than for the low concentration of $CaCl_2$. The amount of precipitated $CaCO_3$ was approximately six times larger in the area occupied by the bacterial solution than in the area occupied by the cementation solution for 0.5 M $CaCl_2$, but it reduced to approximately 1.8 times for 0.1 M $CaCl_2$ and 1.5 times for 0.05 M $CaCl_2$. The distribution of $CaCO_3$ was mainly affected by the distribution of bacteria. A slight difference in the proportion of $CaCO_3$ was observed in three adjacent subareas along the length of the reaction microchannel, implying that surfaces and contacts of sand grains may not offer the preferential nucleation sites for $CaCO_3$ precipitation at the quiescent state.

Data Availability Statement

All data, models, and code generated or used during the study appear in the published article.

Acknowledgments

The authors would also like to acknowledge the financial support from the National Natural Science Foundation of China (Grant Nos. 51922024 and 52078085) and the Natural Science Foundation of Chongqing, China (Grant No. cstc2019jcyjjqX0014). TME was supported by the US National Science Foundation (Grant No. CMMI-1933355) during this work. In addition, Leon A. van Paassen was supported by the Engineering Research Center Program of the US National Science Foundation under NSF (Grant No. ERC-1449501) during this study. Their support is gratefully acknowledged.

Supplemental Materials

Videos S1–S4, Figs. S1–S6, Tables S1–S4, and Eqs. (S1) and (S2) are available online in the ASCE Library (www.ascelibrary.org).

References

Al Qabany, A., and K. Soga. 2013. "Effect of chemical treatment used in MICP on engineering properties of cemented soils." *Géotechnique* 63 (4): 331–339. https://doi.org/10.1680/geot.SIP13.P.022.

Boulos, L., M. Prevost, B. Barbeau, J. Coallier, and R. Desjardins. 1999. "LIVE/DEAD (R) BacLight (TM): Application of a new rapid staining method for direct enumeration of viable and total bacteria in drinking water." *J. Microbiol. Methods* 37 (1): 77–86. https://doi.org/10.1016/S0167-7012(99)00048-2.

Cheng, L., and M. A. Shahin. 2016. "Urease active bioslurry: A novel soil improvement approach based on microbially induced carbonate precipitation." *Can. Geotech. J.* 53 (9): 1376–1385. https://doi.org/10.1139/cgj-2015-0635.

Cheng, L., M. A. Shahin, and D. Mujah. 2017. "Influence of key environmental conditions on microbially induced cementation for soil stabilization." *J. Geotech. Geoenviron. Eng.* 143 (1): 04016083. https://doi.org/10.1061/(ASCE)GT.1943-5606.0001586.

Chou, C.-W., E. A. Seagren, A. H. Aydilek, and M. Lai. 2011. "Biocalcification of sand through ureolysis." *J. Geotech. Geoenviron. Eng.* 137 (12): 1179–1189. https://doi.org/10.1061/(ASCE)GT.1943-5606.0000532.

Chu, J., V. Ivanov, M. Naeimi, V. Stabnikov, and B. Li. 2013. "Microbial method for construction of an aquaculture pond in sand." *Géotechnique* 63 (10): 871–875. https://doi.org/10.1680/geot.SIP13.P.007.

Cui, M., J. Zheng, R. Zhang, H. Lai, and J. Zhang. 2017. "Influence of cementation level on the strength behaviour of bio-cemented sand." *Acta Geotech.* 12 (5): 971–986. https://doi.org/10.1007/s11440-017-0574-9.

Darby, K. M., G. L. Hernandez, J. T. DeJong, R. W. Boulanger, M. G. Gomez, and D. W. Wilson. 2019. "Centrifuge model testing of liquefaction mitigation via microbially induced calcite precipitation." *J. Geotech. Geoenviron. Eng.* 145 (10): 04019084. https://doi.org/10.1061/(ASCE)GT.1943-5606.0002122.

DeJong, J. T., M. B. Fritzges, and K. Nüsslein. 2006. "Microbially induced cementation to control sand response to undrained shear." *J. Geotech. Geoenviron. Eng.* 132 (11): 1381–1392. https://doi.org/10.1061/(ASCE)1090-0241(2006)132:11(1381).

El Mountassir, G., R. J. Lunn, H. Moir, and E. MacLachlan. 2014. "Hydrodynamic coupling in microbially mediated fracture mineralization: Formation of self-organized groundwater flow channels." *Water Resour. Res.* 50 (1): 1–16. https://doi.org/10.1002/2013WR013578.

Fattahi, S. M., A. Soroush, and N. Huang. 2020. "Biocementation control of sand against wind erosion." *J. Geotech. Geoenviron. Eng.* 146 (6): 04020045. https://doi.org/10.1061/(ASCE)GT.1943-5606.0002268.

Feng, K., and B. M. Montoya. 2017. "Quantifying level of microbial-induced cementation for cyclically loaded sand." *J. Geotech. Geoenviron. Eng.* 143 (6): 06017005. https://doi.org/10.1061/(ASCE)GT.1943-5606.0001682.

Foppen, J. W., G. Lutterodt, W. F. M. Roling, and S. Uhlenbrook. 2010. "Towards understanding inter-strain attachment variations of Escherichia coli during transport in saturated quartz sand." *Water Res.* 44 (4): 1202–1212. https://doi.org/10.1016/j.watres.2009.08.034.

Gomez, M. G., C. M. R. Graddy, J. T. DeJong, D. C. Nelson, and M. Tsesarsky. 2018. "Stimulation of native microorganisms for biocementation in samples recovered from field-scale treatment depths."

J. Geotech. Geoenviron. Eng. 144 (1): 04017098. https://doi.org/10.1061/(ASCE)GT.1943-5606.0001804.

Ham, S.-M., I. Chang, D.-H. Noh, T.-H. Kwon, and B. Muhunthan. 2018. "Improvement of surface erosion resistance of sand by microbial biopolymer formation." *J. Geotech. Geoenviron. Eng.* 144 (7): 06018004. https://doi.org/10.1061/(ASCE)GT.1943-5606.0001900.

Harkes, M. P., L. A. van Paassen, J. L. Booster, V. S. Whiffin, and M. C. M. van Loosdrecht. 2010. "Fixation and distribution of bacterial activity in sand to induce carbonate precipitation for ground reinforcement." *Ecol. Eng.* 36 (2): 112–117. https://doi.org/10.1016/j.ecoleng.2009.01.004.

Jiang, N.-J., K. Soga, and M. Kuo. 2017. "Microbially induced carbonate precipitation for seepage-induced internal erosion control in sand-clay mixtures." *J. Geotech. Geoenviron. Eng.* 143 (3): 04016100. https://doi.org/10.1061/(ASCE)GT.1943-5606.0001559.

Kim, D. H., N. Mahabadi, J. Jang, and L. A. van Paassen. 2020. "Assessing the kinetics and pore-scale characteristics of biological calcium carbonate precipitation in porous media using a microfluidic chip experiment." *Water Resour. Res.* 56 (2): e2019WR025420. https://doi.org/10.1029/2019WR025420.

Kim, Y. C. 1996. "Diffusivity of bacteria." *Korean J. Chem. Eng.* 13 (3): 282–287. https://doi.org/10.1007/BF02705951.

Licata, N. A., B. Mohari, C. Fuqua, and S. Setayeshgar. 2016. "Diffusion of Bacterial cells in porous media." *Biophys. J.* 110 (1): 247–257. https://doi.org/10.1016/j.bpj.2015.09.035.

Lin, H., M. T. Suleiman, D. G. Brown, and E. Kavazanjian Jr. 2016. "Mechanical behavior of sands treated by microbially induced carbonate precipitation." *J. Geotech. Geoenviron. Eng.* 142 (2): 04015066. https://doi.org/10.1061/(ASCE)GT.1943-5606.0001383.

Lin, H., M. T. Suleiman, H. M. Jabbour, D. G. Brown, and E. Kavazanjian Jr. 2016b. "Enhancing the axial compression response of pervious concrete ground improvement piles using biogrouting." *J. Geotech. Geoenviron. Eng.* 142 (10): 04016045. https://doi.org/10.1061/(ASCE)GT.1943-5606.0001515.

Liu, L., H. Liu, A. W. Stuedlein, T. M. Evans, and Y. Xiao. 2019. "Strength, stiffness, and microstructure characteristics of biocemented calcareous sand." *Can. Geotech. J.* 56 (10): 1502–1513. https://doi.org/10.1139/cgj-2018-0007.

Mahawish, A., A. Bouazza, and W. P. Gates. 2019a. "Factors affecting the bio-cementing process of coarse sand." *Proc. Inst. Civ. Eng. Ground Improv.* 172 (1): 25–36. https://doi.org/10.1680/jgrim.17.00039.

Mahawish, A., A. Bouazza, and W. P. Gates. 2019b. "Unconfined compressive strength and visualization of the microstructure of coarse sand subjected to different biocementation levels." *J. Geotech. Geoenviron. Eng.* 145 (8): 04019033. https://doi.org/10.1061/(ASCE)GT.1943-5606.0002066.

Martinez, A., L. Huang, and M. G. Gomez. 2019. "Thermal conductivity of MICP-treated sands at varying degrees of saturation." *Geotech. Lett.* 9 (1): 15–21. https://doi.org/10.1680/jgele.18.00126.

Martinez, B. C., J. T. DeJong, T. R. Ginn, B. M. Montoya, T. H. Barkouki, C. Hunt, B. Tanyu, and D. Major. 2013. "Experimental optimization of microbial-induced carbonate precipitation for soil improvement." *J. Geotech. Geoenviron. Eng.* 139 (4): 587–598. https://doi.org/10.1061/(ASCE)GT.1943-5606.0000787.

Minto, J. M., R. J. Lunn, and G. El Mountassir. 2019. "Development of a reactive transport model for field-scale simulation of microbially induced carbonate precipitation." *Water Resour. Res.* 55 (8): 7229–7245. https://doi.org/10.1029/2019WR025153.

Montoya, B. M., and J. T. DeJong. 2015. "Stress-strain behavior of sands cemented by microbially induced calcite precipitation." *J. Geotech. Geoenviron. Eng.* 141 (6): 04015019. https://doi.org/10.1061/(ASCE)GT.1943-5606.0001302.

Montoya, B. M., J. T. DeJong, and R. W. Boulanger. 2013. "Dynamic response of liquefiable sand improved by microbial-induced calcite precipitation." *Géotechnique* 63 (4): 302–312. https://doi.org/10.1680/geot.SIP13.P.019.

Montoya, B. M., S. Safavizadeh, and M. A. Gabr. 2019. "Enhancement of coal ash compressibility parameters using microbial-induced carbonate precipitation." *J. Geotech. Geoenviron. Eng.* 145 (5): 04019018. https://doi.org/10.1061/(ASCE)GT.1943-5606.0002036.

Nayanthara, P. G. N., A. B. N. Dassanayake, K. Nakashima, and S. Kawasaki. 2019. "Microbial induced carbonate precipitation using a native inland bacterium for beach sand stabilization in nearshore areas." *Appl. Sci.* 9 (15): 3201. https://doi.org/10.3390/app9153201.

O'Donnell, T. S., B. E. Rittmann, and E. Kavazanjian Jr. 2017. "MIDP: Liquefaction mitigation via microbial denitrification as a two-stage process. I: Desaturation." *J. Geotech. Geoenviron. Eng.* 143 (12): 04017094. https://doi.org/10.1061/(ASCE)GT.1943-5606.0001818.

Okumus, B., C. J. Baker, J. Carlos Arias-Castro, G. C. Lai, E. Leoncini, S. Bakshi, S. Luro, D. Landgraf, and J. Paulsson. 2018. "Single-cell microscopy of suspension cultures using a microfluidics-assisted cell screening platform." *Nat. Protoc.* 13 (1): 170–194. https://doi.org/10.1038/nprot.2017.127.

Riveros, G. A., and A. Sadrekarimi. 2020. "Liquefaction resistance of Fraser River sand improved by a microbially-induced cementation." *Soil Dyn. Earthquake Eng.* 131 (Apr): 106034. https://doi.org/10.1016/j.soildyn.2020.106034.

Robertson, J., C. McGoverin, F. Vanholsbeeck, and S. Swift. 2019. "Optimisation of the protocol for the LIVE/DEAD (R) BacLight (TM) bacterial viability kit for rapid determination of bacterial load." *Front Microbiol* 10: 801. https://doi.org/10.3389/fmicb.2019.00801.

Rossy, T., C. D. Nadell, and A. Persat. 2019. "Cellular advective-diffusion drives the emergence of bacterial surface colonization patterns and heterogeneity." *Nat. Commun.* 10 (1): 2471. https://doi.org/10.1038/s41467-019-10469-6.

Singh, R., M. Sivaguru, G. A. Fried, B. W. Fouke, R. A. Sanford, M. Carrera, and C. J. Werth. 2017. "Real rock-microfluidic flow cell: A test bed for real-time in situ analysis of flow, transport, and reaction in a subsurface reactive transport environment." *J. Contam. Hydrol.* 204 (Sep): 28–39. https://doi.org/10.1016/j.jconhyd.2017.08.001.

Song, W., F. Ogunbanwo, M. Steinsbo, M. A. Ferno, and A. R. Kovscek. 2018. "Mechanisms of multiphase reactive flow using biogenically calcite-functionalized micromodels." *Lab Chip* 18 (24): 3881–3891. https://doi.org/10.1039/C8LC00793D.

Tobler, D. J., J. M. Minto, G. El Mountassir, R. J. Lunn, and V. R. Phoenix. 2018. "Microscale analysis of fractured rock sealed with microbially induced $CaCO_3$ precipitation: Influence on hydraulic and mechanical performance." *Water Resour. Res.* 54 (10): 8295–8308. https://doi.org/10.1029/2018WR023032.

Torkzaban, S., S. S. Tazehkand, S. L. Walker, and S. A. Bradford. 2008. "Transport and fate of bacteria in porous media: Coupled effects of chemical conditions and pore space geometry." *Water Resour. Res.* 44 (4): W04403. https://doi.org/10.1029/2007WR006541.

van Paassen, L. A. 2009. "Biogrout, ground improvement by microbial induced carbonate precipitation." Ph.D. thesis, Dept. of Biotechnology, Delft Univ. of Technology.

van Paassen, L. A., C. M. Daza, M. Staal, D. Y. Sorokin, W. van der Zon, and M. C. M. van Loosdrecht. 2010a. "Potential soil reinforcement by biological denitrification." *Ecol. Eng.* 36 (2): 168–175. https://doi.org/10.1016/j.ecoleng.2009.03.026.

van Paassen, L. A., R. Ghose, T. J. M. van der Linden, W. R. L. van der Star, and M. C. M. van Loosdrecht. 2010b. "Quantifying biomediated ground improvement by ureolysis: Large-scale biogrout experiment." *J. Geotech. Geoenviron. Eng.* 136 (12): 1721–1728. https://doi.org/10.1061/(ASCE)GT.1943-5606.0000382.

Venda Oliveira, P. J., M. S. da Costa, J. N. P. Costa, and M. Fernanda Nobre. 2015. "Comparison of the ability of two bacteria to improve the behavior of sandy soil." *J. Mater. Civ. Eng.* 27 (1): 06014025. https://doi.org/10.1061/(ASCE)MT.1943-5533.0001138.

Venuleo, S., L. Laloui, D. Terzis, T. Hueckel, and M. Hassan. 2016. "Microbially induced calcite precipitation effect on soil thermal conductivity." *Geotech. Lett.* 6 (1): 39–44. https://doi.org/10.1680/jgele.15.00125.

Wang, K., J. Chu, S. Wu, and J. He. 2020. "Stress-strain behaviour of bio-desaturated sand under undrained monotonic and cyclic loading." *Géotechnique* 71 (6): 521–533. https://doi.org/10.1680/jgeot.19.P.080.

Wang, Y., K. Soga, J. T. DeJong, and A. J. Kabla. 2019a. "A microfluidic chip and its use in characterising the particle-scale behaviour of microbial-induced calcium carbonate precipitation (MICP)." *Géotechnique* 69 (12): 1086–1094. https://doi.org/10.1680/jgeot.18.P.031.

Wang, Y., K. Soga, J. T. DeJong, and A. J. Kabla. 2019b. "Microscale visualization of microbial-induced calcium carbonate precipitation processes." *J. Geotech. Geoenviron. Eng.* 145 (9): 04019045. https://doi.org/10.1061/(ASCE)GT.1943-5606.0002079.

Whiffin, V. S., L. A. van Paassen, and M. P. Harkes. 2007. "Microbial carbonate precipitation as a soil improvement technique." *Geomicrobiol. J.* 24 (5): 417–423. https://doi.org/10.1080/01490450701436505.

Xiao, P., H. Liu, A. W. Stuedlein, T. M. Evans, and Y. Xiao. 2019a. "Effect of relative density and biocementation on the cyclic response of calcareous sand." *Can. Geotech. J.* 56 (12): 1849–1862. https://doi.org/10.1139/cgj-2018-0573.

Xiao, Y., H. Chen, A. W. Stuedlein, T. M. Evans, J. Chu, L. Cheng, N. Jiang, H. Lin, H. Liu, and H. M. Aboel-Naga. 2020a. "Restraint of particle breakage by biotreatment method." *J. Geotech. Geoenviron. Eng.* 146 (11): 04020123. https://doi.org/10.1061/(ASCE)GT.1943-5606.0002384.

Xiao, Y., A. W. Stuedlein, Z. Pan, H. Liu, T. M. Evans, X. He, H. Lin, J. Chu, and L. A. van Paassen. 2020b. "Toe bearing capacity of precast concrete piles through biogrouting improvement." *J. Geotech. Geoenviron. Eng.* 146 (12): 06020026. https://doi.org/10.1061/(ASCE)GT.1943-5606.0002404.

Xiao, Y., A. W. Stuedlein, J. Ran, T. M. Evans, L. Cheng, H. Liu, L. A. van Paassen, and J. Chu. 2019b. "Effect of particle shape on strength and stiffness of biocemented glass beads." *J. Geotech. Geoenviron. Eng.* 145 (11): 06019016. https://doi.org/10.1061/(ASCE)GT.1943-5606.0002165.

Xiao, Y., Z. Zhang, A. W. Stuedlein, and T. M. Evans. 2021. "Liquefaction modeling for biocemented calcareous sand." *J. Geotech. Geoenviron. Eng.* 147 (12): 04021149. https://doi.org/10.1061/(ASCE)GT.1943-5606.0002666.

Yoon, H., K. N. Chojnicki, and M. J. Martinez. 2019. "Pore-scale analysis of calcium carbonate precipitation and dissolution kinetics in a microfluidic device." *Environ. Sci. Technol.* 53 (24): 14233–14242. https://doi.org/10.1021/acs.est.9b01634.

Zhang, C., K. Dehoff, N. Hess, M. Oostrom, T. W. Wietsma, A. J. Valocchi, B. W. Fouke, and C. J. Werth. 2010. "Pore-scale study of transverse mixing induced $CaCO_3$ precipitation and permeability reduction in a model subsurface sedimentary system." *Environ. Sci. Technol.* 44 (20): 7833–7838. https://doi.org/10.1021/es1019788.